International Journal of Heat and Mass Transfer 135 (2019) 62–71

Contents lists available at ScienceDirect

International Journal of Heat and Mass Transfer

journal homepage: www.elsevier.com/locate/ijhmt

# Solute convection effects on a bubble entrapped as a pore during unidirectional upward solidification

P.S. Wei *, C.E. Tsai, T.W. Tseng, L.J. Chen, S.B. Wang, W.S. Lo, K.C. Liao

*Department of Mechanical and Electro-Mechanical Engineering, National Sun Yat-Sen University, Kaohsiung 80424, Taiwan, ROC*

ARTICLE INFO

*Article history:*
Received 23 November 2017
Received in revised form 14 December 2018
Accepted 12 January 2019
Available online 1 February 2019

*Keywords:*
Solute convection
Pore shape
Bubble entrapment
Phase field modelling
Solidification

ABSTRACT

A transport model is proposed to predict entrapment of a bubble during unidirectional upward solidification. Pore formation and its shape in solid influence not only microstructure of materials, but also contemporary issues of various sciences of biology, engineering, foods, geophysics and climate change, etc. In this study, COMSOL computer code is used to solve conservation equations of mass, momentum, energy and solute concentration in liquid, gas and solid phases satisfied by their interfacial conditions. It shows that strong convection deflects the pore growth toward the downstream direction. Time for bubble entrapment, however, depends on the ratio between square of concentration boundary layer thickness and solute diffusivity. Concentration boundary layer thickness is proportional to solute diffusivity divided by difference in bubble growth rate and vertical component of fluid velocity at the bubble cap. The latter is almost independent of incoming horizontal flow. Solute diffusion is therefore the mechanism responsible for bubble entrapment, where the bubble growth rate and vertical velocity component of fluid at the bubble cap are of the same order of magnitude. A triangle region with local high concentration is also found to occur in solid region near the triple-phase line. Predicted contact angle agrees with that obtained from the Abel's equation of the first kind during solidification. This work provides a general model for a fundamental and systematical understanding of mechanisms of a bubble entrapped as a pore in solid.

© 2019 Elsevier Ltd. All rights reserved.

## 1. Introduction

Pore formation and its shape in solid influence not only microstructure of materials, but also contemporary issues of sciences of biology, engineering, foods, geophysics and climate change, etc. Pore formation has been studied in different areas including welding [1–5], casting [6–8], phase change materials [9,10], lotus-type porous materials [11–14], selective laser melting [15], and so on. Actual pore morphology strongly controls properties such as fatigue strength [16], Young's moduli, tensile strength, compressive yield strength, energy absorption, thermal and electrical conductivities of the alloy castings, etc. [13]. Influence of morphology of the pore enhances as product decreases its size.

The predictions of the pore shape should account for different length scales between the pore size and wavelength of deformation of the solidification front, resulting from different transport processes. In the cases of constrained growth of the pore in the mushy zone [17–27], or pore radius around the same magnitude as wavelength of deformation of the solidification front, the pore shape and development during casting of aluminum alloys from a number of models, ranging from analytic solutions to highly complex simulations of evolving porosity and microstructure with stochastic nucleation and growth were reviewed by Lee et al. [22]. Each of models has limitations such as: (1) analytic solutions are applicable only to directional solidification [23]; (2) criteria functions cannot be extrapolated to new alloys or processes [24]; (3) computational models using Darcy's law only show a good correlation to experiment for percentage porosity, not pore morphology [25]; (4) hydrogen diffusion models only predict average values [26]; and (5) continuum-stochastic models [27], which predicted the distribution of porosity and maximum pore size are computationally very expensive.

As wavelength increases or deformation of the solidification front reduces, pore formation is resulting from engulfment of a bubble by a solidification front rather than constrained growth of a bubble in the mushy zone [28–37]. Entrapment of a bubble during unidirectional solidification in the absence of the mushy zone is a process often encountered in manufacturing lotus-type porous materials [11,38,39], crystal growth [40], isolated pores in the welding or joining of pure metals or alloys containing minor impurities [1,4], freezing of sea ice [41], etc. Hadji [30] thus proposed a steady-state model including the lubrication equation of a thin

* Corresponding author.
*E-mail addresses:* pswei@mail.nsysu.edu.tw (P.S. Wei), m043020058@student.nsysu.edu.tw (T.W. Tseng), ljchen@mail.nsysu.edu.tw (L.J. Chen).

https://doi.org/10.1016/j.ijheatmasstransfer.2019.01.060
0017-9310/© 2019 Elsevier Ltd. All rights reserved.

**Nomenclature**

| | |
|---|---|
| C | concentration, mol/m$^3$ |
| $C_{const}$ | high value constant |
| $c_p$ | specific heat, J/kg K |
| D | solute diffusivity, m$^2$/s |
| f | fraction |
| g | gravitation acceleration, m/s$^2$ |
| h | liquid layer thickness, m |
| G | liquid temperature gradient, K/m |
| k | thermal conductivity, W/m-K |
| K | Henry's law constant, Pa m$^3$/mol |
| $k_p$ | equilibrium partition coefficient |
| L | latent heat, J/kg |
| M | molecular weight |
| **n** | normal vector |
| p | pressure, Pa |
| $R_u$ | universal gas constant, J/mol K |
| R(0) | apex radius, m |
| s | solidification front location, m |
| t | time, s |
| T | temperature, K |
| u | velocity component in x direction, m/s |
| U | solidification rate, m/s |
| **v** | velocity vector = u**i** + w**j**, m/s |
| $Vf_g$ | gas fraction = $(1-\phi)/2$ |
| $Vf_{mat}$ | condense material fraction = $(1+\phi)/2$ |
| $\mathbf{V_{in}}$ | interface velocity, m/s |
| w | velocity component in y direction, m/s |
| x | coordinate, m |
| X | mole fraction |
| y | coordinate, m |

*Greek letters*

| | |
|---|---|
| $\mu$ | dynamic viscosity, kg/m-s |
| $\phi$ | phase field function, $\phi = 1$ for metal, $\phi = -1$ for gas |
| $\rho$ | density, kg/m$^3$ |
| $\Delta T_m$ | fictitious temperature range across melting temperature, K |
| $\kappa$ | curvature, 1/m |
| $\theta$ | contact angle, degree |
| $\omega$ | mobility, sm$^3$/kg |
| $\gamma$ | surface tension, N/m |
| $\chi$ | variable $\equiv \omega/\varepsilon^2$, sm/kg |
| $\delta_c$ | thickness of concentration boundary layer, m |
| $\nu$ | kinematic viscosity, m$^2$/s |
| $\delta(n-n_{\ell g})$ | delta function, 1/m |
| $\varepsilon$ | interface thickness, m |
| $\lambda$ | mixing energy density, N |
| $\psi$ | auxiliary variable, defined in Eq. (15) |

*Subscripts*

| | |
|---|---|
| a | atmosphere |
| c | characteristic quantity |
| g | gas |
| i | interface |
| $\ell$ | liquid |
| Liquidus | liquidus |
| m | melting point |
| mat | condensed material |
| n | direction normal to bubble cap |
| s | solid |
| total | total |
| 0 | initial state |

liquid layer and heat conduction equations in the liquid and particle to examine bubble engulfment or relative magnitude between bubble size and wavelength of the deformed solidification front. By accounting for a spherical bubble in a fixed shape (and a SiC solid particle), interface morphology depended on solidification rate, thermal gradient, gap thickness, and thermal conductivities of the bubble and liquid. In the case of a large gap thickness of $10^{-8}$ m, for example, the solidification front was convex due to vanished thermal conductivity of the bubble. An increase in solidification rate greater than 40 μm/s resulted in depression on the elevated part of the solidification front. The trough widened as solidification rate increased, indicating that an increase in solidification rate strongly deformed the solidification front and decreased bubble radius. The analysis also showed that bubble engulfment or rejection depends primarily on competition between hydrodynamic and thermal forces. Park et al. [32] also analytically studied capture of a spherical bubble (or an insoluble particle, a solid particle) submerged in a liquid and approached by an advancing solidification front. Using asymptotic analysis and lubrication approximation, the behavior of the bubble in a fixed spherical shape and deformation of the solidification front were determined by an interplay among gap thickness, thermal conductivity differences between the bubble and liquid, solid–liquid interfacial energy, density change due to liquid–solid phase transition, and Marangoni effect at the liquid–gas interface. A small gas-to-liquid thermal conductivity ratio resulted in repulsion of the bubble away from the solidification front. Deformation of the solidification front depends on the capillary length-to-bubble radius ratio or relative magnitudes between bubble size and wavelength of deformation of the solidification front, and gas-to-liquid thermal conductivity ratio. Capillary length represents the ratio between the variation in temperature due to surface tension and imposed temperature across the bubble radius. There exist convex and concave-convex solidification fronts for gas-to-liquid thermal conductivity ratio less than unity. A small capillary length-to-bubble radius ratio gives rise to a convex solidification front. The concave-convex solidification front is confined to a narrow range close to unity value of gas-to-liquid thermal conductivity ratio. As the capillary length-to-bubble radius ratio increases, this region becomes wider. The effects of density change, convection due to density change, Gibbs-Thomson effect, thickness of the liquid layer between the bubble and solid, etc. on surface deformation and critical speed responsible for bubble engulfment were also presented. Kao et al. [35] examined the interaction of a spherical bubble in a fixed shape (and a solid or liquid particle) with a propagating solidification front in a binary alloy. Numerical boundary integral and continuation methods were used to determine the critical speed for particle capture, as a function of the system parameters. In view of constitutional undercooling, the presence of solute decreases particle speeds by an order of magnitude below those for a single-component system. Thermal and solutal Marangoni effects played a large role.

A further increase in wavelength of the solidification front, fluid flow plays a significant important role in porosity [1]. Kou [1] and Kou and Wang [42] proposed that bubbles nucleated on the solidification front can be entrapped or escaped, depending on upward and downward directions of fluid flow near the solidification front. Wei and Hsiao [43] then proposed a general equation to predict the shape of an entrapped bubble as a pore during solidification. The governing equations were derived by taking time derivative of the equation of state and substituting solute transport rate across the cap. Instead of solving solute concentration equation, an empirical mass transfer coefficient was introduced to evaluate solute transport across the

bubble cap during solidification. The single model can be generated to two- and three-dimensional development of the pore shape in the presence or absence of the mushy zone, provided that significant effects of solidification rate and mass transfer coefficient are relevantly specified. The empirical mass transfer coefficient, however, depends on fluid flow and solidification rate [44].

In the case of small deformation of the solidification front, Karagadde et al. [45] is the first to propose a rather detailed model to numerically trace the growth and movement of a hydrogen bubble in micro-scale under isolated and free growth conditions in a melt having a hydrogen input around the physical domain at a constant temperature during solidification in aluminum castings. Velocity, temperature and concentration fields were predicted from conservation equations of mass, momentum and concentration of liquid phase, whereas the variation of multiphase domains with time was predicted by the level-set equation. The growth rate of bubble surface in the level-set equation was determined by flow velocity and hydrogen diffusion from liquid into bubble. Extending previous work [45], Karagadde et al. [8] further predicted the growth and engulfment of gas microporosity in the mushy zone during aluminum alloy solidification in downward and horizontal directions. Energy equation were introduced. An explicit enthalpy scheme together with Gibbs-Thomson equation were used to predict the shape of mushy zone, coupled with a level-set method for tracking the hydrogen bubble evolution. The predicted average bubble radius and cooling rate in qualitative were in agreement with that provided by Fang and Granger [46], whereas the predicted solidification front speed versus initial bubble radius were in accordance with scale analysis proposed. Panwisawas et al. [15] also proposed a thermal fluid dynamics model and conducted experiments to study the evolution of pores during selective laser melting of Ti-6Al-4V. The complete fluid flow and energy equations were solved, using the volume-of-fluid (VOF) equation to trace pore shape. The predicted pore shape qualitatively agreed with observed morphologies of the pores affected by fluid flow.

This study is to propose a systematical model to predict solute convection resulting in deformation of a bubble cap entrapped as a pore during unidirectional upward solidification. The model is applicable to the bubble size much smaller than radius of curvature of the solidification front encountered in the absence of constitutional supercooling [47,48] or morphological instability [48,49]. Even though the Reynold number ($\equiv u_c R/\nu$) is smaller than unity [50], high Schmidt number ($\equiv \nu/D_\ell$) [51] indicates that concentration field can be affected by fluid flow around the bubble cap above the solidification front. A more general and relevant model to investigate development of the pore shape affected by fluid flow, heat transfer and concentration coupling with a self-consistent deformation of solidification front is still limited [8,45]. In this work, the commercial software packages COMSOL is used to solve transport equations of mass, momentum, energy, species and phase field equations in liquid, solid and gas phases. This work provides a fundamental and critical step to examine the effects of different working parameters such as solidification rate, directions of solidification, liquid concentration and bubble size at the initial state, etc on controlling of pore shapes and their formation in solid encountered in different manufacturing, materials, medical technologies, etc. in the near future.

## 2. System model and analysis

The present model as illustrated in Fig. 1 predicts transport processes during upward unidirectional solidification of water containing carbon dioxide. Since solubility of solid is much less than that of liquid, carbon dioxide is accumulated ahead of the solidification front. A bubble due to supersaturation readily initiates heterogeneously at a concave region of the solidification front denoted by line BE [38,52–54], because solute concentration in the concave area of the solidification front was higher than that near the convex areas. The pore increases its radius and volume in solid in the direction of solidification. They are attributed to increase in volume due to expansion the bubble cap and the displacement of the solidification front [43]. The bubble cap grows or shrinks, depending on solute transport across the cap in different directions and magnitudes [43]. Provided that the bubble growth-to-solidification rate ratio approaches zero and contact angle is 90 degrees, the bubble can be entrapped as a pore in solid [55]. In this study, bubble radius is chosen to be $10^{-5}$ m [8,45]. The origin of the coordinate system is located at the intersection between the vertical axis of the bubble and bottom boundary CD. The physical domain is specified by horizontal x coordinate ranging from $-6.6\times10^{-5}$ to $2.4\times10^{-4}$ m and vertical y coordinate from 0 to $9\times10^{-5}$ m. The maximum and minimum temperatures are 278 and 270 K in the case of small incoming velocity of $10^{-7}$ m/s, 275 and 270 K in the case of $3\times10^{-2}$ m/s, respectively, imposed at top boundary AF and bottom boundary CD, as listed in Table 1. Initial concentrations in liquid, gas and solid are listed in Table 2. Fluid flow is from the left boundary AB to right boundary EF, leading to redistributions of solute concentration and temperature and deflection of bubble growth. Without loss of generality, the assumptions made are

1. The unsteady system is two-dimensional. This is a weak assumption, which is, however, often used as the first step to reveal mechanisms of a complicated process.
2. A thin liquid layer exists between the pre-existing bubble and solid regions in the early stage during unidirectional upward solidification [28,37,54]. Existence of the liquid layer can be simply deduced by Maeno [54] showing a significant difference in base radius of an air bubble between observation from photographs and estimation from Young-Laplace equation applied in the absence of liquid layer between the air bubble and growing ice surface. The pre-existing bubble in liquid can be heterogeneously nucleated by microscopic roughness of the solidification front [54]. In view of the liquid layer in a thickness around 1 μm and solidification rate around $10^{-3}$ m/s, as can be seen later, complete solidification of the liquid layer is less than 0.001 s. Pore volume beneath the solidification front therefore can be nearly stationary.
3. Solid-liquid temperature is independent of solute concentration. Equilibrium temperature at a solid-liquid interface related to mole fraction of solute gas in liquid is given by [56]

$$X = 1 - \exp\left[\frac{ML_{s\ell}}{R_u}\left(\frac{1}{T_m} - \frac{1}{T_{liquidus}}\right)\right] \tag{1}$$

where the ratio between latent heat and gas constant of water $ML_{s\ell}/R_u = 720$. For a carbon dioxide concentration of 40 mol/m$^3$ or mole fraction X of $7.2\times10^{-4}$ in liquid, Eq. (1) indicates that interface temperature is nearly identical to the normal melting point of pure water, namely, a very small $T_m - T_{liquidus} < 0.07$ K.

4. The solidification front is macroscopically planar. Constitutional supercooling can be evaluated by [1]

$$\frac{G}{U} \geqslant \frac{T_{liquidus} - T_m}{D_\ell} \tag{2}$$

The solidification remains planar, provided that Eq. (2) is satisfied. Otherwise, the cellular or dendritic solidification front or the mushy zone will take place. In this work, the term on the left-hand side of Eq. (2) is $10^8$ Ks/ m$^2$ due to temperature gradient

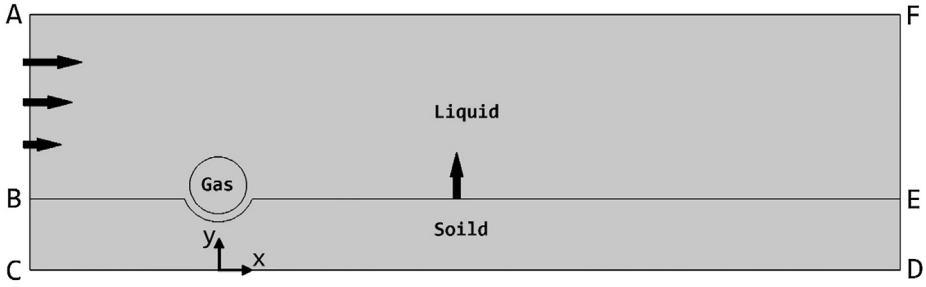


**Fig. 1.** Physical model of unidirectional upward solidification, where boundaries AB, BC, CD, DE, EF, FA stand for entrance location of liquid, solid boundaries at the left-side, bottom and right-side, exit location of liquid, and top of liquid layer, respectively. Line BE is the solidification front.

**Table 1**
Boundary conditions.

| Boundary | C (mol/m$^3$) | p (atm) | T (K) | u (m/s) |
|---|---|---|---|---|
| AB | Eq. (16) | 1 | I.C.[a] | $10^{-7}$ (Low speed)<br>$3\times10^{-2}$, $y \geqslant 6\times10^{-5}$(m)<br>$3\times10^{-2}\left[\frac{2\lvert y-2.5\times10^{-5}\rvert}{3.5\times10^{-5}}-\left(\frac{y-2.5\times10^{-5}}{3.5\times10^{-5}}\right)^2\right]$, $y < 6\times10^{-5}$(m)<br>(High speed) |
| BC | $10^{-3}$ | 1 | I.C. | – |
| CD | $10^{-3}$ | 1 | 270 | – |
| DE | $10^{-3}$ | 1 | I.C. | – |
| EF | Eq. (16) | 1 | I.C. | – |
| AF | Eq. (16) | 1 | 278 or 275 | – |

[a] Same as initial condition.

**Table 2**
Initial conditions.

| | C (mol/m$^3$) | p (atm) | T (K) |
|---|---|---|---|
| Liquid | Eq. (16) | 1 | $273+(278-273)y^{-2.0252}/(8\times10^{-5})^2$<br>or $273+(275-273)y^{-2}/(8\times10^{-5})^2$ |
| Gas | Eq. (17) | 1.2 | $272.5+(273.5-272.5)y^{-1.1}/(2\times10^{-5})^{1.1}$ |
| Solid | $10^{-3}$ | 1 | $270+(273-270)y^{-0.8}/(2.5\times10^{-5})^{0.8}$ |

and solidification rate around $10^5$ K/m and $10^{-3}$ m/s, respectively, whereas the term on the right-hand side is $7\times10^7$ Ks/m$^2$ due to a small temperature range $T_m - T_{liquidus} < 0.07$ K across the interface, as described in previous Assumption 3.

With the above assumptions, conservation equations of mass and momentum equations become

$$\frac{\partial\rho}{\partial t}+\nabla\cdot\rho\mathbf{v}=0 \tag{3}$$

$$\rho\left(\frac{\partial\mathbf{v}}{\partial t}+\mathbf{v}\cdot\nabla\mathbf{v}\right)=-\nabla p+\nabla\cdot\left[\mu(\nabla\mathbf{v}+(\nabla\mathbf{v})^{T})-\frac{2}{3}\mu(\nabla\cdot\mathbf{v})\mathbf{I}\right]+\rho\mathbf{g}+\left[-\gamma\kappa\mathbf{n}+\frac{\partial\gamma}{\partial T}(\nabla T-(\mathbf{n}\cdot\nabla T)\mathbf{n})+\frac{\partial\gamma}{\partial C}(\nabla C-(\mathbf{n}\cdot\nabla C)\mathbf{n})\right]\cdot\mathbf{I}\delta(n-n_{\ell g}) \tag{4}$$

where normal unit vector, curvature and delta function are, respectively,

$$\mathbf{n}=\frac{\nabla\phi}{|\nabla\phi|},\quad \kappa=\nabla\cdot\mathbf{n},\quad \delta=\frac{3}{4}(1-\phi^2)|\nabla\phi| \tag{5}$$

Energy equation is given by

$$\frac{\partial\rho c_p T}{\partial t}+\nabla\cdot\rho c_p\mathbf{v}T=\nabla\cdot(k\nabla T)-\left(\frac{\partial\rho L_{total}}{\partial t}+\nabla\cdot\rho\mathbf{v}L_{total}\right) \tag{6}$$

where the last two terms on the right-hand side represent evolution of latent heat. Latent heat $L_{total} = Lf_\ell$ where liquid fraction is given by

$$f_\ell(T)=\frac{1}{2}\left[1+\tanh\left(\frac{T-T_m}{\Delta T_m}\right)\right] \tag{7}$$

Eq. (7) indicates that liquid and solid are referred to $T > T_m + \Delta T_m/2$ for $f_\ell = 1$ and $T < T_m - \Delta T_m/2$ for $f_\ell = 0$, respectively. The temperature range across the solidification front $\Delta T_m$ is chosen to be 0.12 K, which is a fictitious temperature range across the solid-liquid interface in order to assure convergence of a sudden change in predicting liquid or solid fraction. The fictitious range of temperature is 1.5% of difference between the highest and lowest temperature of the system. Values of the fictitious temperature range were changed and checked to confirm convergence of temperature and other transport variables. Conservation equation of solute is given by

$$\frac{\partial C}{\partial t}+\nabla\cdot\mathbf{v}C=\nabla\cdot(D\nabla C)-(1-k_p)Cf_\ell\frac{\partial f_\ell}{\partial t}Vf_{mat}-\left(\frac{p_g}{R_uT}-\frac{p_g}{K}\right)(\mathbf{v}-\mathbf{V_{in}})\cdot\mathbf{n}\delta(n-n_{\ell g})Vf_{mat}+C_{const}Vf_g\left(\frac{p_g}{R_uT}-C_g\right) \tag{8}$$

where the second and third terms on the right-hand side represent solute generations due to segregation across the solidification front, and partition across the moving bubble cap, respectively. The term for solute segregation at the solidification front appears for $\delta(n-n_{\ell g}) = 0$, $Vf_{mat} = 1$ (and $Vf_g = 0$), whereas that for solute partition across the bubble cap exists for $f_\ell = 1$ and $Vf_{mat} = 1$ (and $Vf_g = 0$). The last term with a chosen constant $C_{const} \to \infty$ together with $Vf_g = 1$ (and $Vf_{mat} = 0$) is introduced to satisfy the equation of state, $p_g/R_uT = C_g$, in the pore. Solute generation at the bubble cap is related to the difference in solute diffusions in the pore and liquid by [57,58]

$$\left(\frac{p_g}{R_u T}-\frac{p_g}{K}\right)(\mathbf{v}-\mathbf{V_{in}})\cdot\mathbf{n}=\mathbf{n}\cdot D_\ell\nabla C_\ell-\mathbf{n}\cdot D_g\nabla C_g \tag{9}$$

where the term on the left-hand side represents solute generation due to difference in velocities between liquid and bubble cap and solute partition across the bubble cap, whereas two terms on the right-hand side represent diffusions in liquid and pore, respectively. Regardless of high solute diffusivity leading to a uniform distribution of solute, solute diffusion in the pore is usually neglected [8,45], as can be seen later. Using Eq. (9) relative velocity between liquid and bubble cap in Eq. (8) gives

$$(\mathbf{v}-\mathbf{V_{in}})\cdot\mathbf{n}\approx\frac{\mathbf{n}\cdot D_\ell\nabla C_\ell}{\frac{p_g}{R_u T}-\frac{p_g}{K}} \tag{10}$$

Eq. (10) is different from the absolute interface velocity considered by Karagadde et al. [8,45]. Local properties in Eqs. (3), (4), (6) and (8) applicable in gas and condensed material phases can be expressed as

$$\begin{pmatrix}\rho\\ k\\ \mu\\ c_p\\ D\end{pmatrix}=Vf_g\begin{pmatrix}\rho_g\\ k_g\\ \mu_g\\ c_{p,g}\\ D_g\end{pmatrix}+Vf_{mat}\begin{pmatrix}\rho_{mat}\\ k_{mat}\\ \mu_{mat}\\ c_{p,mat}\\ D_{mat}\end{pmatrix} \tag{11}$$

where properties of condensed material including liquid and solid phases are given by

$$\begin{pmatrix}\rho_{mat}\\ k_{mat}\\ \mu_{mat}\\ c_{p,mat}\\ D_{mat}\end{pmatrix}=\begin{pmatrix}\rho_s\\ k_s\\ \mu_s\\ c_{p,s}\\ D_s\end{pmatrix}+f_\ell\begin{pmatrix}\rho_\ell-\rho_s\\ k_\ell-k_s\\ \mu_\ell-\mu_s\\ c_{p,\ell}-c_{p,s}\\ D_\ell-D_s\end{pmatrix} \tag{12}$$

Eq. (11) indicates that density, thermal conductivity, viscosity, specific heat and solute diffusivity of the entire system can be referred to solute gas in the pore and condensed material if fraction of gas $Vf_g = 1$ (and $Vf_{mat} = 0$) and condense material $Vf_{mat} = 1$ (and $Vf_g = 0$), respectively. Eq. (12) by substituting Eq. (7) further distinguishes properties of condensed material into those of solid and liquid phases for liquid fraction $f_\ell = 0$ and 1, respectively. Governing Eqs. (3), (4), (6) and (8) therefore can be used to solve transport variables in gas, liquid and solid phases. Phase field equation used to determine surface deformation is given by [59]

$$\frac{\partial\phi}{\partial t}+(\mathbf{v}+(\mathbf{V_{in}}-\mathbf{v}))\cdot\nabla\phi=\nabla\cdot\left\{\frac{\omega\lambda}{\varepsilon^2}\nabla[-\nabla\cdot(\varepsilon^2\nabla\phi)+(\phi^2-1)\phi]\right\} \tag{13}$$

which can be discomposed into two second order partial differential equations

$$\frac{\partial\phi}{\partial t}+(\mathbf{v}+(\mathbf{V_{in}}-\mathbf{v}))\cdot\nabla\phi=\nabla\cdot\left(\frac{\omega\lambda}{\varepsilon^2}\nabla\psi\right) \tag{14}$$

$$-\nabla\cdot(\varepsilon^2\nabla\phi)+(\phi^2-1)\phi\equiv\psi \tag{15}$$

Terms on the left-hand side of Eq. (13) represent the motion of the interface, while the term on the right-hand side is responsible for numerical stabilization and reinitialization. Quantity $\omega$ is the mobility, $\lambda$ is the mixing energy density, and $\varepsilon$ is the interface thickness parameter. The mixing energy density and the interface thickness are related to the surface tension through the relation $\gamma = 2\sqrt{2}\lambda/3\varepsilon$. A variable $\chi$ is linked with the mobility and interface thickness by the relation $\chi = \omega/\varepsilon^2$. For inadequate parameter sets of $\varepsilon$, $\chi$, maximum element size, an excessive diffusion can be observed. The parameter $\chi$ must be as small as possible. In this work, the module of laminar two-phase flow, phase field in COMSOL Multiphase version 5.2 was utilized to solve continuity and momentum Eqs. (3) and (4), and phase field Eqs. (14) and (15), whereas the modules of heat transfer in fluids and transport of diluted species were used to solve energy Eq. (6) and concentration Eq. (8). To assure feasibility and convergence of computation, variable $\chi < 0.01$, whereas interface thickness parameter is $\varepsilon = 8\times10^{-7}$ m. The grid points of $4.6\times10^5$ were used to assure convergence. The relative error was less than 1%.

## 3. Results and discussion

In this study, the effects of convection on the shape of a pore resulting from an entrapped bubble during upward unidirectional solidification of water containing carbon dioxide are numerically and theoretically investigated. Two velocities profiles are considered at entrance location denoted by line AB (see Fig. 1 and Table 1). They are, respectively, $10^{-7}$ velocity and a parabolic velocity profile with the maximum velocity of $3\times10^{-2}$ m/s at the top. Initial temperature profiles in liquid, gas and solid are chosen to be slightly linear (see Table 2). Solidification rate can be estimated to be around $10^{-3}$ m/s by considering energy balance between heat conduction of around $10^5$W/m$^2$ and latent heat evolution during solidification. Initial solute gas pressure in the pore (see Table 2) is related to solute concentration and temperature by the equation of state and the Young-Laplace equation including a given surrounding pressure at top boundary AF. A relevant initial temperature of 292 K in the pore can be estimated from the equation of state $p_{g0} = \rho_{g0}RT_{g0} = 49$ mol/m$^3$)$\times$ 0.044 (kg/mol) $\times$ 190 (J/kg K) $\times$ 292 (K) $= 1.2\times10^5$(N/m$^2$), satisfied by the Young-Laplace equation $p_{g0} = p_a + \rho gh + 2\gamma/R_0 = 10^5 + 0.1 + 2\times0.076/10^{-5} = 1.2\times10^5$N/m$^2$. Initial concentrations of carbon dioxide in liquid can be determined by the Henry's law [60]

$$C_{\ell0}=\frac{1}{K}\left(p_a+\rho gh+\frac{2\gamma}{R_0}\right) \tag{16}$$

Since Henry's law coefficient K = 2900 m$^3$ Pa/mol [60], Eq. (16) gives initial carbon dioxide concentration in water of around 40 mol/m$^3$. Initial carbon dioxide concentration in the pore yields

$$C_{g0}=\frac{p_{g0}}{R_u T_m} \tag{17}$$

which is the equation of state. Initial carbon dioxide concentration in the pore is therefore 49 mol/m$^3$. It should be noted that computer codes are usually suffered from starting computations due to different initial and boundary conditions and models. Iterations of initial conditions are therefore provided in COMSOL code. Discrepancies induced by initial conditions can be damped as time increases.

Significant effects of fluid flow on concentration fields can be revealed by checking the product of Reynolds and Schmidt numbers ($\equiv(u_c R/\nu_\ell)(\nu_\ell/D_\ell)$). In the case of water containing carbon dioxide with liquid solute diffusivity of $10^{-9}$ m$^2$/s, flow velocity of $10^{-2}$ m/s and bubble radius of $10^{-5}$ m, the product of Reynolds and Schmidt number is of a magnitude of around 100. Even though fluid flow is slightly asymmetric with respect to the vertical axis of the bubble cap due to small Reynolds number [50], the concentration boundary layer due to high Schmidt number exhibits asymmetric solute transport and related pressure difference across the bubble cap. Deformation of bubble cap and pore shape is enhanced as time increases. Bubbles on the solidification front in some cases can also be detached due to fluid flow [1].

Fig. 2(a) shows the effects of meshes on convergence of a solute concentration profile along the vertical centerline of the pore. In view of a rapid change in solute concentration, meshes were dense near the bubble cap and growth direction of the pore. Satisfactory convergence of concentration can be reached for the number of meshes greater than $4.6 \times 10^5$, which was chosen in this work. The predicted time-dependent apex radius and solute gas pressure in the pore agree with the Young-Laplace equation during solidification, as shown in Fig. 2(b). Successful agreement also confirms appropriate sizes of meshes near interfaces. The Abel's equation of the first or second kind was found to be the general equation governing development of contact angle of a tiny bubble cap responsible for the pore shape [55]. Fig. 3 shows that predicted contact angle as a function of solidification front location agrees with the solution of the Abel's equation of the first or second kind. The latter was in good agreement with experimental results [61].

The pore shapes affected by fluid flow with the maximum velocity of $3 \times 10^{-2}$ m/s at the top of the entrance location at times of 0.0006 s and 0.0015s are shown in Fig. 4(a) and 4(b),

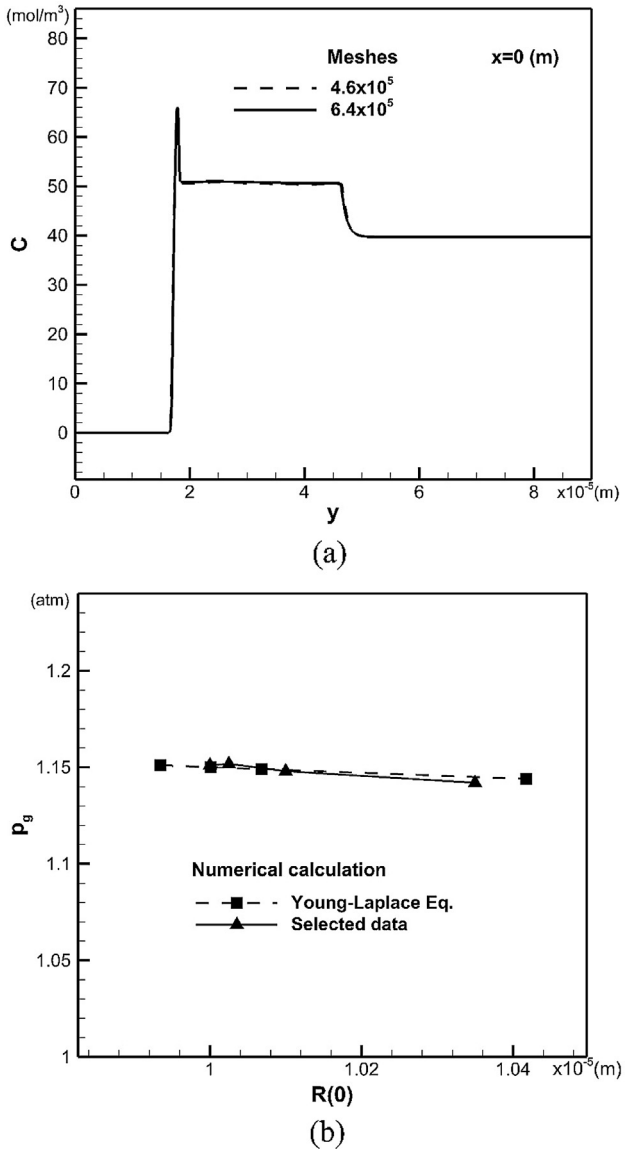


**Fig. 2.** Convergence test of (a) a concentration profile along vertical centerline of the pore for different meshes, and (b) predicted solute gas pressure versus apex radius in the pore in comparison with Young-Laplace equation.

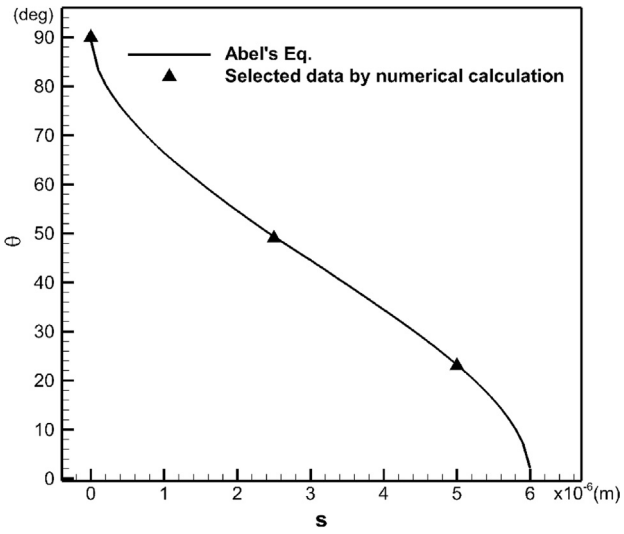


**Fig. 3.** Predicted contact angle in comparison with solutions of Abel's Eq. of the first or second kind during solidification.

respectively. Different colors represent different densities of phases. The white line delineates the boundary of pore. It can be seen that the flow becomes upwards as flow approaches the bubble. In view of stronger flow, the direction of bubble growth is deviated toward downstream locations. The bubble will be entrapped in solid after time becomes much greater than 0.0027 s, as shown in Fig. 4(c). The time scale for bubble entrapment is thus of the order of around $10^{-3}$ s. Since solute diffusivity is usually $0.01\sim 10^{-3}$ of kinematic viscosity in liquid, thickness of the concentration boundary layer is much less than that of momentum boundary layer. Considering a developing concentration boundary layer, the change in concentration with time is thus balanced by solute diffusion. Time scale then yields

$$t_c \sim \frac{\delta_{\ell c}^2}{D_\ell} \tag{18}$$

Since concentration boundary layer thickness is around $10^{-6}$ m (see Fig. 2(a)), time for bubble entrapment scaled by Eq. (18) gives $10^{-3}$ s. The predicted and measured concentration boundary layer thickness can also be 0.0003 m near a solidification location of 0.001 m [62]. Prediction from Eq. (18) therefore gives time for bubble entrapment of the order of 100 s, agreeing with experimental measurements [62]. For a greater thickness of 0.003 m and solidification rate around $10^{-6}$ m/s time scale for bubble entrapment estimated from Eq. (18) gives a longer time around $10^4$ s [63].

Concentration boundary layer thickness, however, can be scaled from conservation of solute transport across the bubble cap from Eq. (10). That is,

$$\delta_{\ell c} \sim \frac{D_\ell}{V_{inc} - v_{nc}} \tag{19}$$

Since solute diffusivity in liquid is very small, Eq. (19) indicates vertical velocity component of liquid to be of the same order of magnitude as growth rate of the bubble cap. Combining Eqs. (18) and (19) therefore indicates that solute diffusion is the mechanism responsible for time of bubble entrapment. In the case of vertical velocity component around $10^{-3}$ m/s, concentration boundary layer thickness from Eq. (19) successfully gives $10^{-6}$ m. Measured thickness of concentration boundary layers of 0.0003 m in [62] can also be interpreted by Eq. (19) subject to measured solidification rates of around $3 \times 10^{-6}$ m/s, respectively. Vertical velocity compo-

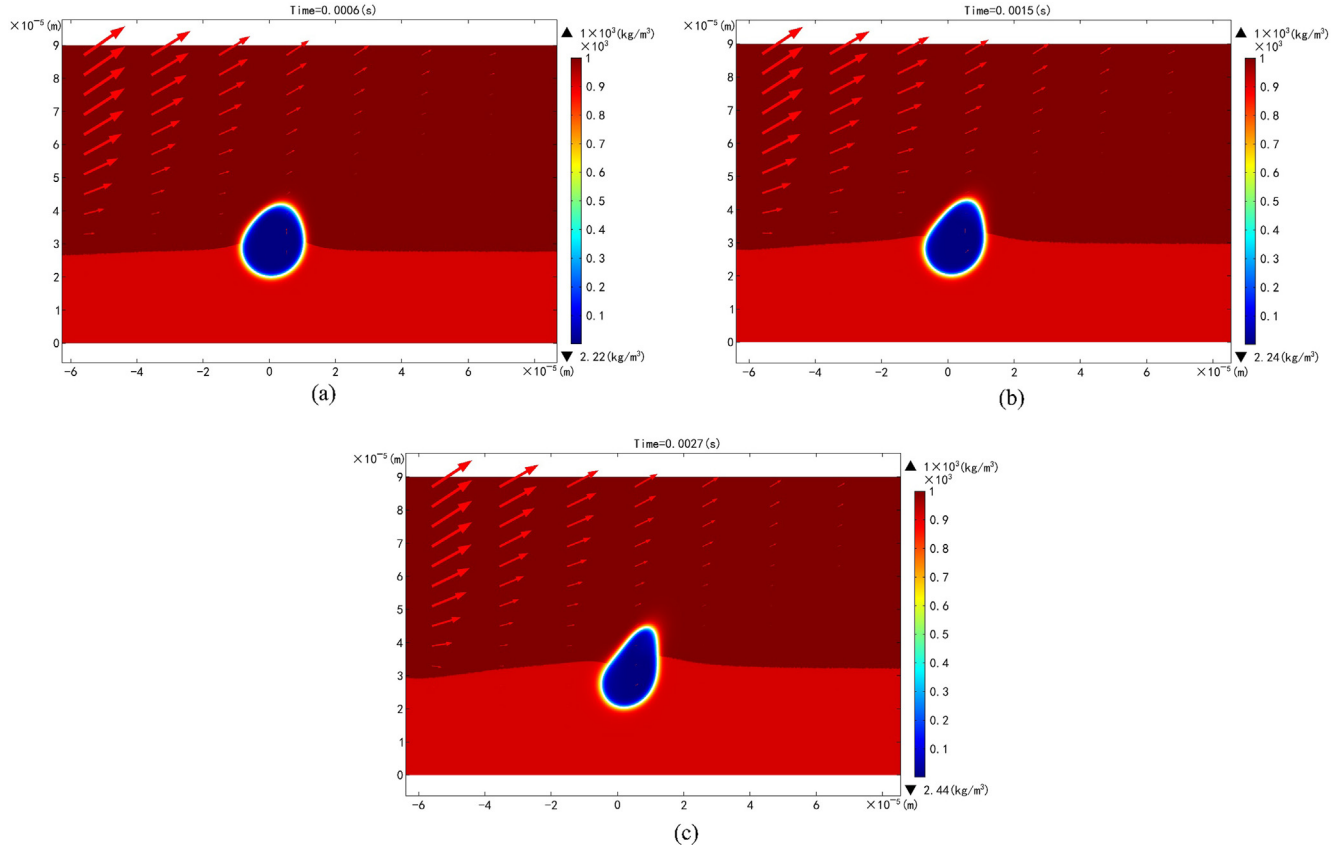


**Fig. 4.** Velocity fields around the pore in a portion of the domain at times of (a) 0.0006 s, (b) 0.0015 s, and (c) 0.0027 s for a parabolic velocity distribution with the maximum velocity of $3 \times 10^{-2}$ m/s at the top of entrance location. The white line represents the pore boundary.

nent of fluid near the bubble cap is of the same order of relative velocity between the bubble cap and fluid for different times, as shown in Fig. 5. The relative vertical velocity component between the bubble cap and fluid flow or solute transport across the bubble cap decreases as time increases. It is interesting to find that vertical velocity component of liquid can be $10^{-3}$ m/s. Since the incoming velocity is $10^{-7}$ m/s, the velocity field induced is a result of the difference in pressures across the bubble cap. Difference in pressures across the bubble cap is bigger than that from the entrance to exit locations.

The corresponding pore shape together with concentration field at a time of 0.0006 s is shown in Fig. 6(a). Solute concentration in the pore is relatively constant with a high value around 50 mol/m$^3$, whereas iso-concentrations are of circular shapes around the bubble cap. Solute concentration drops rapidly in the liquid or solid near the pore (see Fig. 2), and then decreases concentration as distance from the bubble surface increases. Interestingly, there exist local maximum regions in a triangle shape in the solid near the triple- phase line, rather than that on the bubble cap and solidification front. This is attributed to accumulations of solute diffusion from the pore to surrounding liquid and solute rejection via liquid-solid transition. Iso-concentration lines are flat and parallel to the solidification front away from the bubble. Fig. 6(b) and (c) show concentration around the bubble in the liquid spreads as time increases. In view of continuous accumulation, the region with highest concentration expands as time increases. In view of incoming flow, distributions of concentration exhibit asymmetric patterns. The spread of the region with highest concentration in the rear is longer than that in the front. Concentration in solid maintains the same shape for different times, since solute diffusivity in solid is very small.

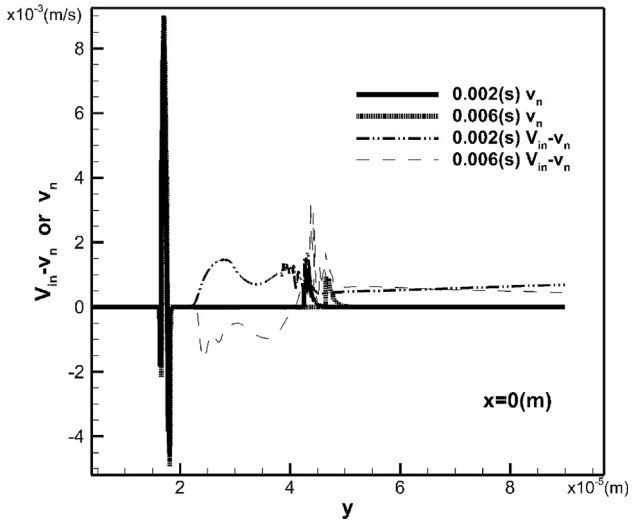


**Fig. 5.** Velocity component of fluid and relative velocity component between bubble cap and fluid along the vertical centerline of the pore subject to incoming negligible velocity at times of 0.002 s and 0.006 s.

Fig. 7 shows concentration profiles along the vertical centerline of the pore for different times and negligible velocity at the entrance location. Solute concentration in the pore is relatively constant. Solute diffusion in the pore can be therefore neglected, as mentioned previously. Aside from strong circulation of gas flow, uniformity of solute gas concentration in the pore is attributed to high solubility of solute gas in the pore and solute transport from

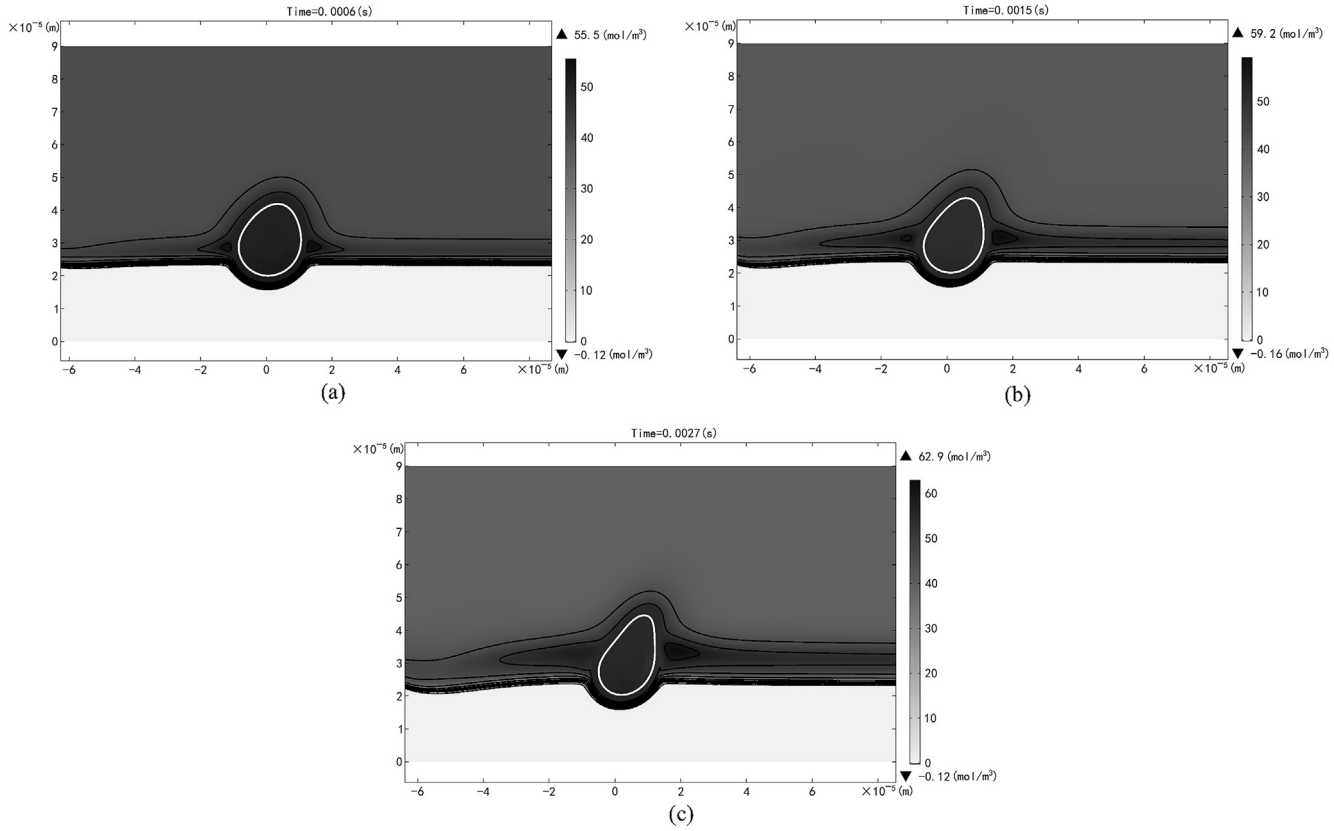


**Fig. 6.** The corresponding pore shapes together with concentration field in a portion of the domain at times of (a) 0.0006 s, (b) 0.0015 s, and (c) 0.0027 s for a parabolic velocity distribution with the maximum velocity of $3 \times 10^{-2}$ m/s at the top of entrance location. The white line represents the pore boundary.

the pore to surrounding liquid. Since distance for solute gas diffusion in the pore $\delta_{gc} \sim \sqrt{D_g t}$, as mentioned previously, distance for solute diffusion is of the order of $10^{-4}$ m, which is ten times greater than radius of the pore. A jump of concentration near the bottom of the pore is a consequence of adjustment of initial conditions. It decreases as time increases. Solute concentration drops rapidly in the liquid around the pore. Concentration around the bubble in the liquid spreads as time increases. Distance for solute diffusion in liquid is around $10^{-6}$ m during 0.01 s, which is about thickness of concentration boundary layer shown in this figure. Solute concentration in solid is frozen due to very small solute diffusivity. The effects of solute Marangoni force on velocity fields are insignificant, as shown in Fig. 8. Contradiction between previous work [32,34,35] and this study is a consequence of small differences in concentration along the bubble cap. Driving forces such as capillary pressure, thermal and solute Marangoni forces are balanced by

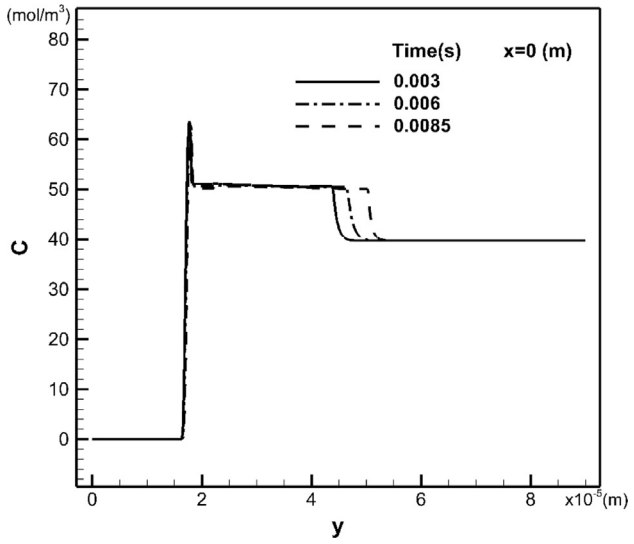


**Fig. 7.** Concentration profiles along the vertical centerline of the pore at different times subject to negligible velocity at entrance location.

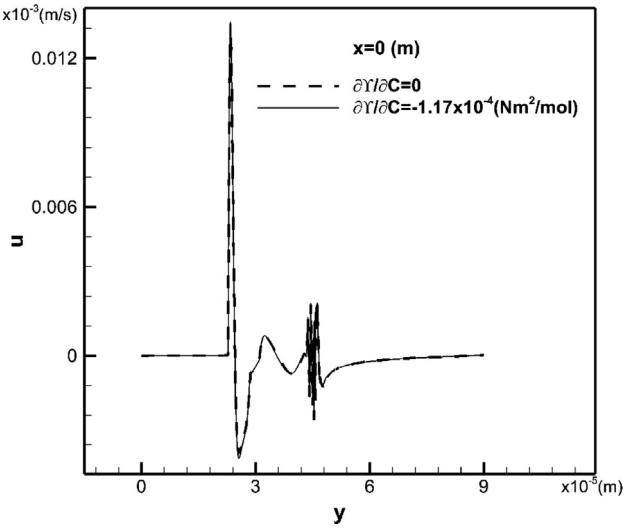


**Fig. 8.** Effects of capillary force due to solute concentration on horizontal velocity component along the vertical centerline of the pore.

shear stress and included in the Navier-Stokes Eq. (4). The effects of fluid flow and shear stress on the pore shape are thus automatically accounted for. It can be seen that velocities near the bubble cap exhibit oscillations and opposite directions. In order to maintain balance of shear stresses across the liquid-gas interface, opposite directions of tangential velocity are required to compensate significant difference in dynamic viscosities between liquid and gas. On the other hand, velocity is sensitive to changes in direction and magnitude due to significant difference in densities between liquid and gas

## 4. Conclusions

Conclusions drawn are the followings:

1. This study provides a rigorous model accounting for mass, momentum, energy and concentration transport in distinct phases to predict and reveal mechanisms of development of the pore shape in solid during solidification. Scale analysis is also presented to interpret computed and experimental results.
2. The flow becomes upwards as the bubble is approached. In the case of stronger flow, the bubble is deviated in the downstream direction.
3. Time scale for bubble entrapment is confirmed to be proportional to square of concentration boundary layer thickness divided by solute diffusivity. The former is scaled by the ratio between solute diffusivity and difference in vertical component of velocities between bubble cap and fluid flow at the bubble cap.
4. Vertical fluid flow at the bubble cap is nearly independent of horizontal liquid flow parallel to the solidification front. This is attributed to higher pressure difference across the bubble cap.
5. Solute diffusion is the mechanism responsible for bubble entrapment. In view of low solute diffusivity in liquid, vertical component of fluid flow near the bubble cap is of the same order of magnitude as bubble growth rate.
6. Solute concentration in the pore is nearly constant. There exists a triangle region with local maximum concentration in solid near the triple-phase line, as a result of solute accumulation via diffusion from the pore to liquid and rejection from liquid-solid phase transition. In view of convection, the shape of triangle region is more elongated in the rear than that in the front.
7. The effects of solute Marangoni force on velocity fields are insignificant.
8. Predicted contact angle of the bubble cap during solidification agrees with that predicted by Abel's equation of the first or second kind, which was found to agree with experimental data.

## Conflict of interest

The authors declared that there is no conflict of interest.

## Acknowledgement

The work is financially supported by NSC 102-2221-E-110-038.

## References

[1] S. Kou, Welding Metallurgy, second ed., Wiley, New York, 2003.
[2] J.L. Huang, N. Warnken, J. Gebelin, M. Strangwood, R.C. Reed, On the mechanism of porosity formation during welding of titanium alloys, Acta Mater. 60 (2012) 3215–3225.
[3] J.W. Elmer, J. Vaja, H.D. Carlton, R. Pong, The effect of Ar and $N_2$ shielding gas on laser weld porosity in steel, stainless steels, and nickel, Weld. J. 94 (2015), 313-s-325-s.
[4] J.J. Blecher, T.A. Palmer, T. DebRoy, Porosity in thick section alloy 690 welds – experiments, modeling, mechanism, and remedy, Weld. J. 95 (2016), 17-s-26-s.
[5] J.E. Ramirez, B. Han, S. Liu, Effect of welding variables and solidification substructure on weld metal porosity, Metall. Mater. Trans. A 25 (1994) 2285–2294.
[6] R. Hardin, C. Beckermann, Effect of porosity on the stiffness of cast steel, Metall. Mater. Trans. A 38 (2007) 2992–3006.
[7] P.D. Lee, J.D. Hunt, Hydrogen porosity in directionally solidified aluminum–copper alloys: in situ observation, Acta Mater. 45 (1997) 4155–4169.
[8] S. Karagadde, S. Sundarraj, P. Dutta, A model for growth and engulfment of gas microporosity during aluminum alloy solidification process, Comput. Mater. Sci. 65 (2012) 383–394.
[9] C.D. Sulfredge, L.C. Chow, K.A. Tagavi, Void initiation and growth in unidirectional freezing: the influence of natural convection, Exper. Heat Transfer 6 (1993) 411–436.
[10] K. Tagavi, L.C. Chow, O. Solaiappan, Void formation in unidirectional solidification, Exper. Heat Transfer 3 (1990) 239–255.
[11] K. Yoshimura, T. Inada, S. Koyama, Growth of spherical and cylindrical oxygen bubbles at an ice-water interface, Cryst. Growth Des. 8 (2008) 2108–2115.
[12] Y. Liu, Y.X. Li, J. Wan, H.W. Zhang, Evaluation of porosity in lotus-type porous magnesium fabricated by metal/gas eutectic unidirectional solidification, Mater. Sci. Eng. A. 402 (2005) 47–54.
[13] H. Nakajima, Fabrication, properties and application of porous metals with directional pores, Prog. Mater. Sci. 52 (2007) 1091–1173.
[14] L. Drenchev, J. Sobczak, N. Sobczak, W. Sha, S. Malinov, A comprehensive model of ordered porosity formation, Acta Mater. 55 (2007) 6459–6471.
[15] C. Panwisawas, C.L. Qiu, Y. Sovani, J.W. Brooks, M.M. Attallah, H.C. Basoalto, On the role of thermal fluid dynamics into the evolution of porosity during selective laser melting, Scr. Mater. 105 (2015) 14–17.
[16] Q.G. Wang, P.E. Jones, Prediction of fatigue performance in aluminum shape castings containing defects, Metall. Mater. Trans. B 38 (2007) 615–621.
[17] P.D. Lee, J.D. Hunt, Hydrogen porosity in directionally solidified aluminum–copper alloys: a mathematical model, Acta Mater. 49 (2001) 1383–1398.
[18] Ch. Pequet, M. Gremaud, M. Rappaz, Modeling of microporosity, macroporosity, and pipe-shrinkage formation during the solidification of alloys using a mushy-zone refinement method: applications to aluminum alloys, Metall. Mater. Trans. A 33 (2002) 2095–2106.
[19] M.F. Zhu, Z.Y. Li, D. An, Q.Y. Zhang, T. Dai, Cellular automation modeling of microporosity formation during solidification of aluminum alloys, ISIJ Int. 54 (2014) 384–391.
[20] H. Meidani, A. Jacot, Phase-field simulation of micropores constrained by the dendritic network during solidification, Acta Mater. 59 (2011) 3032–3040.
[21] H. Meidani, J.L. Desbiolles, A. Jacot, M. Rappaz, Three-dimensional phase-field simulation of micropore during solidification: morphological analysis and pinching effect, Acta Mater. 60 (2012) 2518–2527.
[22] P.D. Lee, A. Chirazi, D. See, Modeling microporosity in aluminum-silicon alloys: a review, J. Light Metals 1 (2001) 15–30.
[23] T.S. Piwonka, M.C. Flemings, Pore formation in solidification, AIME Met. Soc. Trans. 236 (1966) 1157–1165.
[24] E. Niyama, T. Uchida, M. Morikawa, S. Saito, A method of shrinkage prediction and its application to steel casting practice, AFS Int. Cast Met. J. 9 (1982) 52–63.
[25] Ch. Pequet, M. Rappaz, Modeling of porosity formation during the solidification of aluminum alloys using a mushy zone refinement method, in: Modeling of Casting, Welding and Advanced Solidification Processes, Vol. IX, pp. 71–79, 2000.
[26] R.C. Atwood, S. Sridhar, W. Zhang, P.D. Lee, Diffusion-controlled growth of hydrogen pores in aluminium–silicon castings: in situ observation and modelling, Acta Mater. 48 (2000) 405–417.
[27] J. Huang, J.G. Conley, T. Mori, Simulation of microporosity formation in modified and unmodified A356 alloy castings, Metall. Mater. Trans. B 29 (1998) 1249–1260.
[28] A.A. Chernov, D.E. Temkin, A.M. Mel'nikova, The influence of the thermal conductivity of a macroparticle on its capture by a crystal growing from a melt, Sov. Phys. Crystallogr. 22 (1977) 656–658.
[29] Ya.E. Geguzin, A.S. Dzuba, Crystallization of a gas-saturated melt, J. Cryst. Growth 52 (1981) 337–344.
[30] L. Hadji, Axisymmetric shapes and forces resulting from the interaction of a particle with a solidifying interface, Phys. Rev. E 66 (2002) 041404.
[31] Y. Wang, L.L. Regel, W.R. Wilcox, Can propagation of gas bubbles lead to detached solidification? Experiments on freezing of water, Cryst. Growth Des. 2 (2002) 453–461.
[32] M.S. Park, A.A. Golovin, S.H. Davis, The encapsulation of particles and bubbles by an advancing solidification front, J. Fluid Mech. 560 (2006) 415–436.
[33] D.M. Stefanescu, The multidisciplinary facets of particle engulfment and pushing, Trans. Indian Inst. Met. 60 (2007) 79–86.
[34] L. Hadji, Migration of a bubble in front of a directionally solidified interface, Phys. Rev. E 75 (2007) 042602.
[35] J.C.T. Kao, A.A. Golovin, S.H. Davis, Particle capture in binary solidification, J. Fluid Mech. 625 (2009) 299–320.
[36] G.-R. Jiang, Y.-X. Li, Y. Liu, Influence of solidification mode on pore structure of directionally solidified porous Cu-Mn alloy, Trans. Nonferrous Met. Soc. China 21 (2011) 88–95.
[37] E.A. Ghezal, A. Nehari, K. Lebbou, T. Duffar, Observation of gas bubble incorporation during micropulling-down growth of sapphire, Cryst. Growth Des. 12 (2012) 5715–5719.
[38] K. Murakami, H. Nakajima, Formation of pores during unidirectional solidification of water containing carbon dioxide, Mater. Trans. 43 (2002) 2582–2588.

[39] V. Shapovalov, L. Boyko, Gasar—A new class of porous materials, Adv. Eng. Mater. 6 (2004) 407–410.
[40] Y.-J. Lai, J.-C. Chen, Effects of the laser heating and air bubbles on the morphologies of c-axis $LiNbO_3$ fibers, J. Crys. Growth 231 (2001) 222–229.
[41] S. Deville, Ice-templating, freeze casting: Beyond materials processing, J. Mater. Res. 28 (2013) 2202–2219.
[42] S. Kou, Y.H. Wang, Weld pool convection and its effect, Weld. J. 65 (1986), 63-s-70-s.
[43] P.S. Wei, S.Y. Hsiao, Effects of mass transfer coefficient on pore shape in solid, Int. J. Heat Mass Transfer 103 (2016) 931–939.
[44] P.S. Wei, Y.K. Kuo, S.H. Chiu, C.Y. Ho, Shape of a pore trapped in solid during solidification, Int. J. Heat Mass Transfer 43 (2000) 263–280.
[45] S. Karagadde, S. Sundarraj, P. Dutta, Modeling growth of hydrogen bubbles in aluminum castings using the level-set method, Scr. Mater. 61 (2009) 216–219.
[46] Q.T. Fang, D.A. Granger, Porosity formation in modified and unmodified A356 alloy castings, AFS Trans. 97 (1989) 989–1000.
[47] W. Rutter, B. Chalmers, A prismatic substructure formed during solidification of metals, Can. J. Phys. 31 (1953) 15–39.
[48] P.S. Wei, Thermal science of weld bead defects: a review, ASME J. Heat Transfer 133 (2011) 031005.
[49] W.W. Mullins, R.F. Sekerka, Stability of a planar interface during solidification of a dilute binary alloy, J. Appl. Phys. 35 (1964) 444–451.
[50] H. Schlichting, Boundary-Layer Theory, seventh ed., McGraw-Hill, New York, 1979.
[51] A. Bejan, Convection Heat Transfer, Wiley, New York, 1995, 1984.
[52] P.M. Wilt, Nucleation rates and bubble stability in water-carbon dioxide solutions, J. Colloid Interface Sci. 112 (1986) 530–538.
[53] Ya.E. Geguzin, A.S. Dzyuba, Gas evolution and the formation and capture of gas bubbles at the crystallization front when growing crystals from the melt, Sov. Phys. Crystallogr. 22 (1977) 197–199.
[54] N. Maeno, Air bubble formation in ice crystals, in: H. Oura (ed.), Physics of Snow and Ice, Proceedings, Vol. 1, Part 1, Hokkaido University, Sapporo, Japan, 1967, pp. 207–218.
[55] P.S. Wei, S.Y. Hsiao, Pore shape development from a bubble captured by a solidification front, Int. J. Heat Mass Transfer 55 (2012) 8129–8138.
[56] S.M. Walas, Phase Equilibria Chemical Engineering, Butterworth Pub, Boston, 1985.
[57] S. Kou, Transport Phenomena and Materials Processing, Wiley, New York, 1996.
[58] C.J. Forster, M.K. Smith, The transient modeling of single bubble nucleate boiling in a sub-cooled liquid using an ALE moving mesh, in: Excerpt from the Proceedings of the 2011 COMSOL Conference in Boston, 2011.
[59] Y. Sun, C. Beckermann, Sharp interface tracking using the phase-field equation, J. Comput. Phys. 220 (2007) 626–653.
[60] Henry's law, <https://en.wikipedia.org/wiki/Henry%27s_law>.
[61] P.S. Wei, C.C. Chang, Existence of universal phase diagrams for describing general pore shape resulting from an entrapped bubble during solidification, ASME J. Heat Transfer 138 (2016) 104503.
[62] P.S. Wei, C.C. Huang, Z.P. Wang, K.Y. Chen, C.H. Lin, Growths of bubble/pore sizes in solid during solidification -an in-situ measurement and analysis, J. Cryst. Growth 270 (2004) 662–673.
[63] P.S. Wei, C.C. Huang, K.W. Lee, Nucleation of bubbles on a solidification front-experiment and analysis, Metall. Mater. Trans. B 34 (2003) 321–332.